Supporting Information

Telluride-based atomically thin layers of ternary 2D transition metal dichalcogenide alloys

Amey Apte [†], Aravind Krishnamoorthy [‡], Jordan Adam Hachtel [⊥], Sandhya Susarla [†], Juan Carlos Idrbo [⊥], Aiichiro Nakano [‡], Rajiv K. Kalia [‡], Priya Vashishta [‡*], Chandra Sekhar Tiwary [†+*], and Pulickel M. Ajayan [†*]

[†] Department of Materials Science & NanoEngineering, Rice University, 6100 Main St, Houston TX – 77005 USA

[‡] Collaboratory for Advanced Computing and Simulations, Department of Physics and Astronomy, University of Southern California, Los Angeles, CA – 90089 USA

[⊥] Center for Nanophase Materials Science, Oak Ridge National Laboratory, Oak Ridge TN – 37831 USA

[+] Metallurgical and Materials Engineering, Indian Institute of Technology, Kharagpur 721302, West Bengal, India.

Estimation of relative and absolute chalcogen compositions:

For the Alloys A & B, the X-ray photoelectron spectroscopy (XPS) results gave a relative composition (%c) of telluride (to selenium) as 10% and 40% respectively.

Given that the chemical formula of the sample is written as $MoSe_{2(1-x)}Te_{2x}$, we have:

$$\frac{2x}{2(1-x)} = \%c$$

For c = 10%, we have: $\frac{x}{1-x} = 0.1 \; x = \frac{1}{11} = 0.09$

For c = 40%, we have: $\frac{x}{1-x} = 0.4 \;\; x = \frac{4}{14} = 0.28$

Hence, the estimated chemical formulae for Alloys A & B are $MoSe_{1.82}Te_{0.18}$ and $MoSe_{1.44}Te_{0.56}$ respectively.

Stability of the Te-doped samples at ambient conditions after six months:

The pure $MoSe_2$ and Alloy B samples were investigated with Raman and PL spectroscopy six months after synthesis. They were stored at ambient conditions. Fig. S1 shows the Raman and PL spectra. We can see that the samples show little to no difference with the spectra reported in Fig. 1 (manuscript) which were recorded when they were synthesized freshly. The pure $MoSe_2$ samples show strong A_{1g} Raman mode whereas the Alloy B samples show an asymmetric redshift mode which is convolution of the A_{1g} Se-Mo-Te and E_{2g} of 2H Te-Mo-Te

vibrations (discussed in Fig. 5 of manuscript). The maxima of the PL emission of samples (pure $MoSe_2$ ~ 1.56 eV, Alloy B ~ 1.42 eV) are also more or less consistent with the respective values in Fig. 1. Thus, the samples retain good stability in ambient conditions.

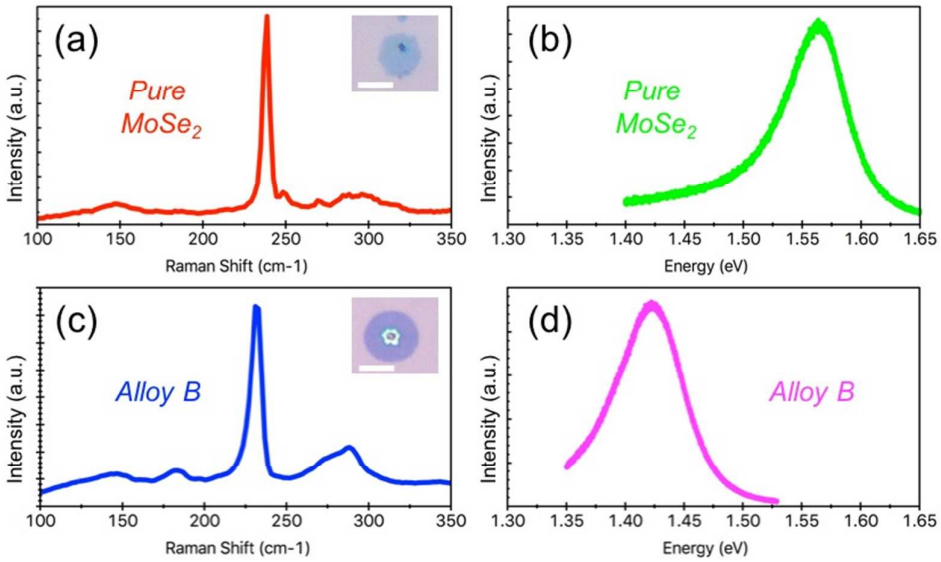

Figure S1 Raman and PL spectra of (a,b) Pure $MoSe_2$ and (c,d) Alloy B respectively. The insets show optical images of the flakes (scale bars = 10 μm).

Table 1: Internal energy and configurational and vibrational free energies of MoSe2(1-x)Te2x structures evaluated at room temperature, T = 300 K. All energies are extensive quantities and evaluated per 108 toms in the simulation cell. The free energy of formation of the fully random alloy is the lowest among the structures considered in this study at -0.26 eV/simulation cell.

System	$\boldsymbol{U}$ **(eV)**	$\boldsymbol{S_{\mathrm{config}}}$	$\boldsymbol{-300K \cdot S_{\mathrm{config}}}$ **(eV)**	$\boldsymbol{-300K \cdot S_{\mathrm{vib}}}$ **(eV)**	$\boldsymbol{\Delta G_f}$ **(eV)**
$MoSe_2$	-747.67	$k_B \ln 1$	0.00	-10.03	----
Heterostructure ($Mo_{36}Se_{24}Te_{48}$)	-699.63	$k_B \ln 1$	0.00	-11.01	+0.96
Partly random ($Mo_{36}Se_{26}Te_{46}$)	-701.66	$k_B \ln \binom{36}{13}$	-0.56	-10.90	+0.31
Fully Random ($Mo_{36}Se_{26}Te_{46}$)	-701.54	$k_B \ln \binom{72}{26}$	-1.16	-10.99	-0.26
$MoTe_2$	-676.85	$k_B \ln 1$	0.00	-11.56	----

Force field parameterization

Molecular dynamics simulations were performed with an empirical Stillinger-Weber forcefield. Containing 2- and 3-body interaction terms, this forcefield has been used previously in MD simulations and studies of thermal and elastic phenomena in transition metal dichalcogenide (TMDC) materials. [1–3] Forcefield parameters for $MoSe_2$ and $MoTe_2$ crystals were optimized using density functional theory calculations of structural properties like lattice constants and vibrational properties like the phonon dispersion curve. Forcefield parametrization was performed with the GULP code, which uses the Broyden-Fletcher-Goldfarb-Shanno algorithm to minimize the objective function [4,5]

$$F(x) = \sum_{i=1}^{N} w_i \left[f_i^{SW}(x) - f_i^{exp-DFT} \right]^2$$

Here, the vector x denotes the Stillinger-Weber parameters, f_i^{obs} is the ith observable quantity, such as lattice constant and vibrational frequency obtained from first-principles DFT calculations. $f_i^{calc}(x)$ is the corresponding value calculated using the Stillinger Weber forcefield with parameters defined by x and w_i is an empirically chosen weight which represents the relative importance of the observable quantity, $f_i^{exp-DFT}$.

The Stillinger-Weber parameters for $MoSe_2$ and WSe_2 crystals used in this study are listed Tables 1 and 2. Tables 3 and 4 compare the structural properties of $MoSe_2$ and $MoTe_2$ calculated by the optimized SW forcefield to values obtained from experiments and DFT simulations. Figure S1 compares the phonon dispersion spectra produced by the MoSe2 and MoTe2 Stillinger-Weber forcefields to those generated from DFT simulations. This figure

demonstrates that lattice vibrations, especially those of low-energy acoustic modes are captured accurately in the Stillinger Weber force field.

Table 2: Stillinger Weber parameters for the $MoSe_2$ crystal.

$$E_{bond}(r) = A \cdot \exp\left(\frac{\rho}{r - r_{max}}\right)\left(\frac{B}{r^4 - 1}\right)$$

Bond	A	ρ	B	r_{max}
Se-Se	2.42	1.675	29.45	4.493
Mo-Se	6.02	0.390	12.60	3.345
Mo-Mo	3.19	0.339	33.30	4.493

$$E_{angle}(r, \theta) = \lambda \cdot \exp\left(\frac{2\gamma}{r - r_{max}}\right)(\cos\theta - \cos\theta_0)^2$$

Angle	λ	θ_0	γ	r_{max}
Se-Mo-Se	66.026	80.833	1.708	3.345
Mo-Se-Mo	23.488	80.833	5.711	3.345

Table 3: Optimized Stillinger Weber parameters for the $MoTe_2$ crystal.

$$E_{bond}(r) = A \cdot \exp\left(\frac{\rho}{r - r_{max}}\right)\left(\frac{B}{r^4 - 1}\right)$$

Bond	A	ρ	B	r_{max}
Te-Te	2.971	2.040	50.10	4.806
Mo-Te	6.644	0.312	13.65	3.590
Mo-Mo	2.773	0.282	38.70	4.806

$$E_{angle}(r,\theta) = \lambda \cdot \exp\left(\frac{2\gamma}{r-r_{max}}\right)(\cos\theta - \cos\theta_0)^2$$

Angle	λ	θ_0	γ	r_{max}
Te-Mo-Te	32.989	80.288	1.935	3.590
Mo-Te-Mo	21.280	80.288	5.711	3.590

Mixed 2-body and 3-body interaction parameters for the alloy, namely Se-Te, Mo-Mo and Se-Mo-Te are taken as linear interpolations of respective terms in the pure $MoSe_2$ and $MoTe_2$ crystals.

Table 4: Comparison of Stillinger Weber structural properties with DFT and experimental values for $MoSe_2$

Quantity	SW forcefield	Experimental/DFT	Error (%)
Lattice constant (a, Å)	3.29	3.3 [6,7]	0.30
Included unit cell angle (γ, °)	120	120	0.00

Table 5: Comparison of Stillinger Weber properties with DFT and experimental values for WSe_2

Quantity	SW forcefield	Experimental/DFT	Error (%)
Lattice constant (a, Å)	3.511	3.519 [8,9]	-0.22
Included unit cell angle (γ, °)	120	120	0.00

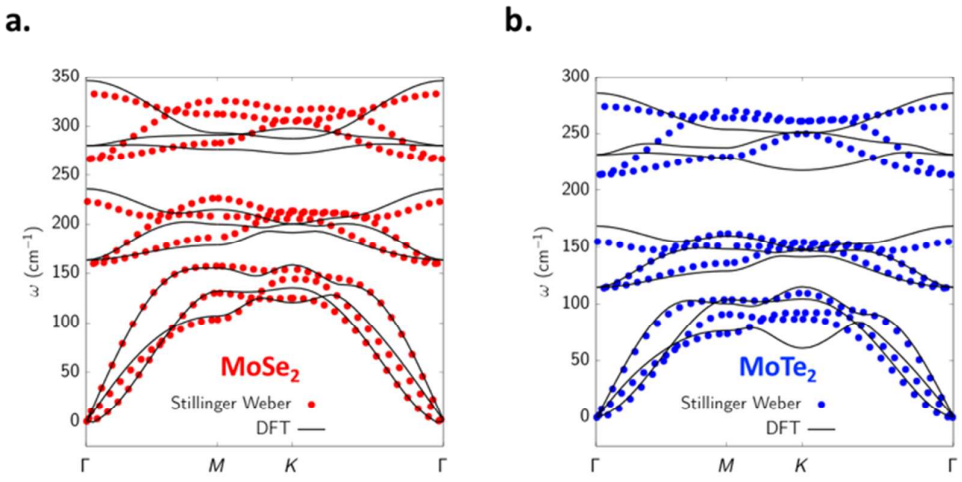

Figure S1: Comparison of phonon dispersion curves of a. $MoSe_2$ and b. $MoTe_2$ monolayers predicted by the Stillinger-Weber forcefield with DFT-predicted values. The good agreement between ab initio and Stillinger-Weber frequencies, particularly for low-lying acoustic vibrations indicates that low and intermediate temperature vibrational properties are well represented by the empirical forcefield.

Electronic structure of $MoSeTe_2$ alloys

The figure below shows the computed band gaps and electronic structure near the Fermi level of (a) pure $MoSe_2$, (b) $MoSe_{2(1-x)}Te_{2x}$ alloy, x = 0.64 and (c) pure $MoTe_2$. We observe a monotonic reduction in the computed band gap with increasing Te content in the $MoSe_{2(1-x)}Te_{2x}$ crystal. This trend is consistent with PL observations of band gap reduction from 1.55 eV in pristine $MoSe_2$ to 1.49 eV in $MoSe_{2(1-x)}Te_{2x}$; x = 0.5 to 1.42 eV in $MoSe_{2(1-x)}Te_{2x}$; x = 0.83. While the relative variations in band gap with Te content are consistent with experiments, all three band gap values are underestimated due to well-known deficiencies with semi-local functionals like PBE used in this calculation.

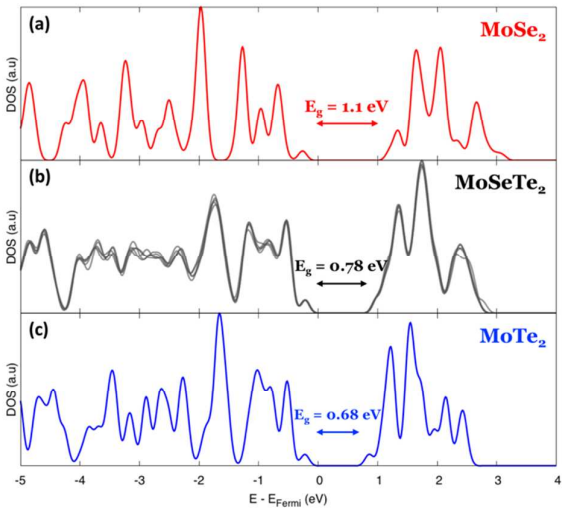

Figure S3: DFT computed band-edge electronic structures for (a) pure $MoSe_2$, (b) $MoSe_{2(1-x)}Te_{2x}$ alloy, x = 0.64 and (c) pure $MoTe_2$ monolayers show a reduction in band gap with increasing Te content. DOS from five different initial atomic configurations of the MoSeTe2 alloy are overlaid in (b). The band gap was found to be insensitive to the distribution of Se/Te ions in the random alloy.

References

(1) Payam, N.; David, J. S. Thermal Conductivity of Single-Layer WSe 2 by a Stillinger–Weber Potential. *Nanotechnology* **2017**, *28*, 075708.

(2) Kandemir, A.; Yapicioglu, H.; Kinaci, A.; Cagin, T.; Sevik, C. Thermal Transport Properties of MoS2 and MoSe2 Monolayers. *Nanotechnology* **2016**, *27*, 055703.

(3) Xiong, S.; Cao, G. X. Bending Response of Single Layer MoS2. *Nanotechnology* **2016**, *27*, 105701.

(4) Gale, J. D. GULP: A Computer Program for the Symmetry-Adapted Simulation of Solids. *J. Chem. Soc. - Faraday Trans.* **1997**, *93*, 629–637.

(5) Shanno, D. F. Conditioning of Quasi-Newton Methods for Function Minimization. *Math. Comput.* **1970**, *24*, 647.

(6) Roy, A.; Movva, H. C. P.; Satpati, B.; Kim, K.; Dey, R.; Rai, A.; Pramanik, T.; Guchhait, S.; Tutuc, E.; Banerjee, S. K. Structural and Electrical Properties of MoTe2 and MoSe2 Grown by Molecular Beam Epitaxy. *ACS Appl. Mater. Interfaces* **2016**, *8*, 7396–7402.

(7) Xenogiannopoulou, E.; et al. High-Quality, Large-Area MoSe2 and MoSe2/Bi2Se3 Heterostructures on AlN(0001)/Si(111) Substrates by Molecular Beam Epitaxy. *Nanoscale* **2015**, *7*, 7896–7905.

(8) Puotinen, D.; Newnham, R. E. The Crystal Structure of MoTe${\sb 2}$. *Acta Crystallogr.* **1961**, *14*, 691–692.

(9) Dawson, W. G.; Bullet, D. W. Electronic Structure and Crystallography of MoTe 2 and WTe 2. *J. Phys. C Solid State Phys.* **1987**, *20*, 6159.